6-1-1997

High-Order Interior Caustics Produced in Scattering of a Diagonally Incident Plane Wave by a Circular Cylinder

Charles L. Adler

James A. Lock
Cleveland State University, j.lock@csuohio.edu

Bradley R. Stone

Claudio J. Garcia

Original Citation

Adler, C. L., James A. Lock, Bradley R. Stone, and Claudio J. Garcia. "High-Order Interior Caustics Produced in Scattering of a Diagonally Incident Plane Wave by a Circular Cylinder." *Journal of the Optical Society of America A: Optics Image Science and Vision* 14 (1997): 1305-1315.

High-order interior caustics produced in scattering of a diagonally incident plane wave by a circular cylinder

C. L. Adler, James A. Lock, Bradley R. Stone, and Claudio J. Garcia

Department of Physics, Cleveland State University, Cleveland, Ohio 44115

Received July 12, 1996; accepted October 28, 1996; revised manuscript received December 3, 1996

We examine scattering of a family of initially parallel diagonally incident rays by a dielectric circular cylinder and show that the interior and exterior caustics that occur are qualitatively identical to those produced at normal incidence. We find, however, that (1) varying the plane-wave tilt angle has the same effect on the caustics as varying the refractive index of the cylinder at normal incidence and (2) high-order interior caustics are visible because of larger internal-reflection Fresnel coefficients at diagonal incidence than at normal incidence. We also observe noncaustic ray trajectories produced by the sharp peaking of internal-reflection Fresnel coefficients at large ray impact parameters, as well as another class of internal caustics produced by scattering from inhomogeneities in our glass cylinder. © 1997 Optical Society of America
[S0740-3232(97)01806-1]

1. INTRODUCTION

In recent years there has been much interest in laboratory observations of the interior and exterior caustics produced when a plane wave or a focused beam is scattered by a sphere or a spheroid. The caustics are parameterized by an integer p denoting the number of internal chords of the ray trajectories; i.e., the family of rays that produces either an interior or exterior caustic has undergone $p - 1$ internal reflections before the caustic is formed. For scattering by a sphere, the most familiar exterior caustic is the $p = 1$ near-zone spherical aberration caustic.[1,2] For $p \geqslant 2$, far-zone rainbow caustics and forward-scattering and backscattering glory caustics occur as well.

There have been two types of laboratory observations of the far-zone rainbow caustics. Sassen[3] experimentally studied the $2 \leqslant p \leqslant 5$ and $p = 7$ rainbows of a spherical water droplet illuminated with laser light by placing a detector in the far zone. Chan and Lee[4] observed most of the far-zone rainbows for $2 \leqslant p \leqslant 24$, as well as the $p = 32$ rainbow, by using this technique. In a different set of experiments, Walker[5–7] observed the colored glare spots corresponding to the $2 \leqslant p \leqslant 14$ rainbows by blocking off a portion of the incident beam and focusing his eye on the surface of a spherical water droplet. Walker's beam-blocking technique allows relatively weak high-order rainbows not to be obscured by the dominant reflected and transmitted light that would otherwise be scattered at the same angle. It has been shown by Lock[8] that scattering of a Gaussian beam focused to a waist much smaller than the diameter of the sphere is equivalent to the beam-blocking technique. Chan and Lee employed this Gaussian-beam technique to observe the very-high-order rainbows. Lock[9] and van de Hulst and Wang[10] have developed the theory of the glare spots, showing that they correspond to sharp peaks in the power spectrum of the far-zone scattered electric field sampled in the vicinity of rainbows. Other types of illumination of the sphere have also been considered. A $p = 1$ far-zone rainbow caustic cannot occur for plane-wave incidence on a sphere.[11,12] But when a point source is brought close to the sphere, the $p = 1$ near-zone spherical aberration caustic splits into two branches and evolves into a far-zone rainbow.[13]

The interior caustics of a sphere include the so-called $p = 1$ Descartes ring, which is the extension of the spherical aberration cusp into the sphere,[14] and various cusp caustics and axial spike caustics[15–17] for $p \geqslant 2$. The $p = 1$ Descartes ring, enhanced by morphology-dependent resonances, has been observed at the surface of both water and methanol droplets by means of stimulated Raman scattering (SRS).[18,19] The interior $p = 2$ cusp caustic and the turning point of the $p = 4$ axial spike caustic have been observed by both SRS[20,21] and by fluorescence of rhodamine 590 dye molecules in water droplets.[2] The full $p = 2$ axial spike caustic has also been observed in a spherical globe filled with water into which a small amount of milk had been added.[15]

For scattering by an oblate spheroidal particle with side-on incidence, the rainbow evolves into a higher-dimensional optical caustic whose full structure unfolds as the spheroid refractive index and eccentricity are varied. The unfolding of this caustic for $p = 2$ has been numerically and analytically explored by Nye,[22,23] and the unfolding as a function of spheroid eccentricity has been experimentally studied by Marston and his co-workers for $p = 2$,[24–27] $p = 3$,[28] and $p = 6$.[29] For scattering by a prolate spheroid with end-on incidence, the $p = 1$ near-zone spherical aberration caustic also evolves into a higher-dimensional optical caustic and has been numerically explored by Lock.[30]

In contrast, there has been relatively little analysis and observation of the interior and exterior caustics of a long circular cylinder illuminated by either a normally or di-

agonally incident plane wave. Perhaps this is because at normal incidence, the interior and exterior caustics are identical to those for a sphere, except for the absence of the interior spike caustics and the far-zone glory caustics produced by the sphere's axial focusing. At normal incidence the interior $p = 1$ Descartes line caustic and the interior $p = 2$ cusp caustic have been theoretically examined in the context of wave theory by Owen *et al.*[31] The $p \geqslant 2$ interior cusp caustics at normal incidence have been described in terms of Airy theory by Steinhardt and Fukshansky.[32] The $p = 1$ cylindrical aberration caustic of a thin fiber at normal incidence has been studied by Benincasa *et al.*[2]

To the best of our knowledge, the caustics produced by a plane wave diagonally incident on a cylinder have not been analyzed in detail. The purposes of this paper and a companion paper[33] are to describe these caustics theoretically and to observe them experimentally. In this paper the caustics are described in terms of ray theory, and various of the $1 \leqslant p \leqslant 6$ interior caustics are observed. In the companion paper, the $p = 2$ far-zone rainbow caustic is described in terms of wave theory and is also observed.

Although the diagonal-incidence caustics are qualitatively identical to those that occur at normal incidence, we find that there are two quantitative differences between them that significantly impact on their observation in the laboratory. First, varying the tilt angle of the plane wave with respect to the cylinder is equivalent to varying the cylinder's refractive index at normal incidence. This makes the unfolding of the caustics easy to observe. Second, the Fresnel coefficients for internal reflection at diagonal incidence are substantially larger than their values at normal incidence. This permits the observation of much-higher-order interior caustics than is possible at normal incidence.

The body of this paper is organized as follows. In Subsection 2.A we define our notation and describe the plane-wave/cylinder geometry. In Subsection 2.B we derive the expressions for the trajectory of a light ray as it propagates through the cylinder, and in Subsection 2.C we derive the expression for the ray's polarization state. In Section 3 we briefly catalog the interior and exterior caustics for various values of p and describe a particular set of caustic transitions. In Section 4 we experimentally observe many of the $1 \leqslant p \leqslant 6$ interior caustics and compare our observations with ray theory predictions. In addition to the caustics cataloged in Section 3, we observe a second set of interior caustics that arise from scattering by inhomogeneities present in our cylindrical glass rod at the focal position of the $p = 1$ cusp caustic. In Section 5 we present our conclusions.

2. RAY THEORY MODEL OF SCATTERING OF A DIAGONALLY INCIDENT PLANE WAVE BY A CIRCULAR CYLINDER

A. Notation and Scattering Geometry

We consider a long dielectric circular cylinder of radius a and refractive index n whose axis coincides with the z axis of a rectangular coordinate system. A monochromatic plane wave of wave number $k = 2\pi/\lambda$ whose propagation direction is in the x–z plane and making an angle ξ with the x axis is incident on the cylinder. This geometry is illustrated in Fig. 1. The interior and scattered rays are numbered by integers $p \geqslant 0$. After the initial interaction of a ray with the cylinder surface (the $p = 0$ interaction), the specularly reflected ray is denoted by $p = 0$, and the portion of the ray transmitted into the cylinder is denoted by $p = 1$. At the next interaction of the transmitted ray with the cylinder surface (the $p = 1$ interaction), the portion of the ray transmitted out of the cylinder is denoted by $p = 1$, the internally reflected portion is denoted by $p = 2$, and so forth.

In wave theory the natural polarization states of the incident plane wave, the interior wave, and the scattered wave are denoted by ϵ and μ. In the ϵ polarization, the wave's electric field is confined to the horizontal (x–y) plane, and in the μ polarization its magnetic field is confined to the horizontal plane. In ray theory the natural polarization states for the interaction of a light ray with a locally flat surface are the transverse electric (TE) and transverse magnetic (TM) states. We find in Subsection 2.C that both polarization-preserving scattering and cross-polarized scattering occur when a plane wave is diagonally incident on a circular cylinder because the ϵ and μ and TE and TM directions do not coincide and because the TE and TM directions for the pth interaction of a ray with the cylinder surface do not coincide with the TE and TM directions for the $(p - 1)$st interaction.

B. Ray Trajectories

Consider a ray diagonally incident on the cylinder as in Fig. 2. The propagation direction of the ray is

$$\hat{k}_{i0} = (\cos \xi)\hat{u}_x - (\sin \xi)\hat{u}_z, \tag{1}$$

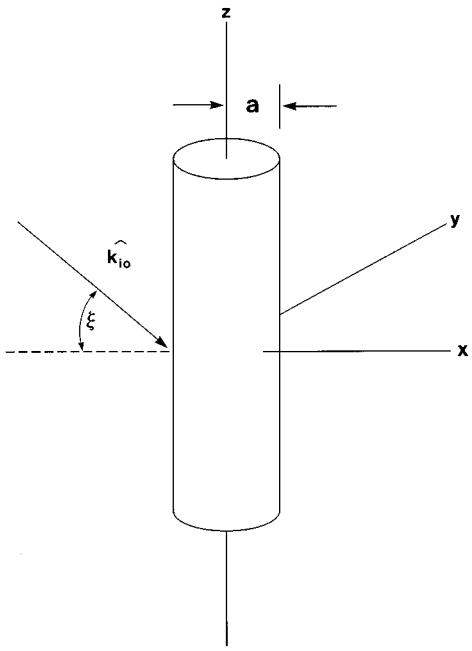

Fig. 1. A plane wave with propagation direction $\hat{k}_{i0}$ in the x–z plane and making an angle ξ with the x axis is incident on a dielectric circular cylinder of radius a.

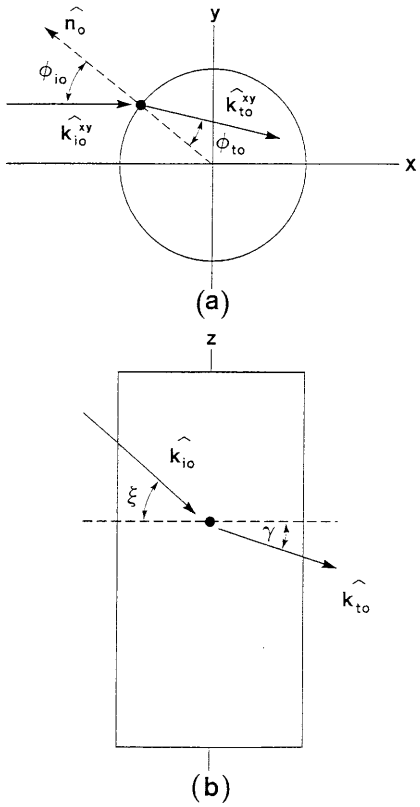

Fig. 2. Trajectory of the incident ray $\hat{k}_{i0}$ and the transmitted ray $\hat{k}_{t0}$ as seen from (a) the top of the cylinder and (b) the side of the cylinder. $\hat{k}_{i0}^{xy}$ and $\hat{k}_{t0}^{xy}$ are the normalized projections of $\hat{k}_{i0}$ and $\hat{k}_{t0}$ in the x–y plane.

where the subscript i denotes incident and the subscript 0 denotes the $p = 0$ interaction of the ray with the surface. The ray strikes the cylinder at the point (x_0, y_0, z_0). The outward normal to the cylinder at this point is

$$\hat{n}_0 = -(\cos\,\phi_{i0})\hat{u}_x + (\sin\,\phi_{i0})\hat{u}_y. \tag{2}$$

The angle of incidence of the ray is then θ_{i0}, where

$$\cos\,\theta_{i0} = -\hat{k}_{i0}\cdot\hat{n}_0 = \cos\,\xi\,\cos\,\phi_{i0}, \tag{3}$$

and the angle of refraction of the ray inside the cylinder is θ_{t0}, where the subscript t denotes transmitted and

$$n\,\sin\,\theta_{t0} = \sin\,\theta_{i0}. \tag{4}$$

The propagation direction of the transmitted ray inside the cylinder is[34]

$$\begin{aligned}\hat{k}_{t0} &= \frac{1}{n}\,\hat{k}_{i0} + \left(\frac{1}{n}\cos\,\theta_{i0} - \cos\,\theta_{t0}\right)\hat{n}_0\\ &= \left[\frac{1}{n}\cos\,\xi - \cos\,\phi_{i0}\left(\frac{1}{n}\cos\,\theta_{i0} - \cos\,\theta_{t0}\right)\right]\hat{u}_x\\ &\quad + \left[(\sin\,\phi_{i0})\left(\frac{1}{n}\cos\,\theta_{i0} - \cos\,\theta_{t0}\right)\right]\hat{u}_y\\ &\quad - \frac{1}{n}\,(\sin\,\xi)\hat{u}_z.\end{aligned} \tag{5}$$

The physical interpretation of Eq. (5) becomes evident if we consider separately the projections of the incident and transmitted rays in the x–y plane and along the z axis. Defining the angles ϕ_{t0} and γ as in Figs. 2(a) and 2(b), respectively, by

$$\cos\,\phi_{t0} = -\hat{k}_{t0}^{xy}\cdot\hat{n}_0, \tag{6}$$

where $\hat{k}_{t0}^{xy}$ is the projection of $\hat{k}_{t0}$ in the x–y plane and normalized to unit magnitude, and

$$n\,\sin\,\gamma = \sin\,\xi, \tag{7}$$

we may write Eq. (5) as

$$\begin{aligned}\hat{k}_{t0} &= [\cos\,\gamma\,\cos(\phi_{i0} - \phi_{t0})]\hat{u}_x\\ &\quad - [\cos\,\gamma\,\sin(\phi_{i0} - \phi_{t0})]\hat{u}_y - (\sin\,\gamma)\hat{u}_z.\end{aligned} \tag{8}$$

As seen from the side, refraction of the incident ray is described by Snell's law through Eq. (7). All subsequent internal reflections occur at the angle γ as well. The final transmission of the ray out of the cylinder occurs at the angle ξ, also in accordance with Eq. (7) and producing the conical wave fronts of the scattered electric field.[35,36]

As seen from above, the angles ϕ_{i0} and ϕ_{t0} are related through substitution of Eqs. (2)–(5), and (7) into Eq. (6) by

$$n'\,\sin\,\phi_{t0} = \sin\,\phi_{i0}, \tag{9}$$

where

$$n' = n\,\cos\,\gamma/\cos\,\xi. \tag{10}$$

The projection of the ray in the horizontal plane also obeys Snell's law if the cylinder interior is associated with the effective refractive index n'. All subsequent internal reflections occur at the angle ϕ_{t0} as well. The final transmitted angle in the horizontal plane of the pth scattered ray is

$$\Theta = (p - 1)\pi + 2\phi_{i0} - 2p\,\phi_{t0}. \tag{11}$$

C. Ray Polarization

If the incident ray is ϵ polarized, its electric and magnetic fields are given by

$$\begin{aligned}\mathbf{E}_{i0}^{\epsilon} &= E_0^{\epsilon}\hat{u}_y = E_0^{\epsilon}\hat{u}_{i0}^{\epsilon},\\ \mathbf{B}_{i0}^{\epsilon} &= \frac{E_0^{\epsilon}}{c}\,[(\sin\,\xi)\hat{u}_x + (\cos\,\xi)\hat{u}_z],\end{aligned} \tag{12}$$

where E_0^{ϵ} is the amplitude of the incident field and $\hat{u}_{i0}^{\epsilon}$ is the ϵ polarization direction. If the incident ray is μ polarized, its fields are given by

$$\begin{aligned}\mathbf{E}_{i0}^{\mu} &= E_0^{\mu}[(\sin\,\xi)\hat{u}_x + (\cos\,\xi)\hat{u}_y] = E_0^{\mu}\hat{u}_{i0}^{\mu},\\ \mathbf{B}_{i0}^{\mu} &= -\frac{E_0^{\mu}}{c}\,\hat{u}_y,\end{aligned} \tag{13}$$

where E_0^{μ} and $\hat{u}_{i0}^{\mu}$ have similar meanings. By constructing the unit vectors in the $\widehat{\mathrm{TE}}_{i0}$ and $\widehat{\mathrm{TM}}_{i0}$ directions according to the prescription

$$\widehat{\mathrm{TE}}_{i0} = \hat{k}_{i0}\times\hat{n}_0/\sin\,\theta_{i0}, \qquad \widehat{\mathrm{TM}}_{i0} = \widehat{\mathrm{TE}}_{i0}\times\hat{k}_{i0}, \tag{14}$$

we find that the ϵ and μ polarization states of the incident ray are rotated with respect to the TE and TM polarization states by

$$\widehat{\mathrm{TM}}_{i0} = (\cos\chi)\hat{u}^{\epsilon}_{i0} - (\sin\chi)\hat{u}^{\mu}_{i0},$$

$$\widehat{\mathrm{TE}}_{i0} = (\sin\chi)\hat{u}^{\epsilon}_{i0} + (\cos\chi)\hat{u}^{\mu}_{i0}, \tag{15}$$

or

$$\begin{pmatrix}\widehat{\mathrm{TM}}_{i0}\\ \widehat{\mathrm{TE}}_{i0}\end{pmatrix} = R(-\chi)\begin{pmatrix}\hat{u}^{\epsilon}_{i0}\\ \hat{u}^{\mu}_{i0}\end{pmatrix}, \tag{16}$$

where the rotation angle χ is given by

$$\cos\chi = \sin\phi_{i0}/\sin\theta_{i0},$$

$$\sin\chi = \sin\xi\cos\phi_{i0}/\sin\theta_{i0} \tag{17}$$

and where R is the two-dimensional rotation matrix

$$R(\psi) = \begin{bmatrix}\cos\psi & \sin\psi\\ -\sin\psi & \cos\psi\end{bmatrix}. \tag{18}$$

The interaction of a light ray with a locally flat interface is diagonal in the TE and TM basis, i.e.,

$$\begin{pmatrix}E^{\mathrm{TM}}_{t0}\\ E^{\mathrm{TE}}_{t0}\end{pmatrix} = \begin{bmatrix}t^{\mathrm{TM}}_0 & 0\\ 0 & t^{\mathrm{TE}}_0\end{bmatrix}\begin{pmatrix}E^{\mathrm{TM}}_{i0}\\ E^{\mathrm{TE}}_{i0}\end{pmatrix} \tag{19}$$

for transmission and

$$\begin{pmatrix}E^{\mathrm{TM}}_{r0}\\ E^{\mathrm{TE}}_{r0}\end{pmatrix} = \begin{bmatrix}r^{\mathrm{TM}}_0 & 0\\ 0 & r^{\mathrm{TE}}_0\end{bmatrix}\begin{pmatrix}E^{\mathrm{TM}}_{i0}\\ E^{\mathrm{TE}}_{i0}\end{pmatrix} \tag{20}$$

for reflection, where t^{TM}_0, r^{TM}_0 and t^{TE}_0, r^{TE}_0 are the flat-interface transmission and reflection Fresnel coefficients for TM and TE, respectively, evaluated at the $p = 0$ interface. After the transmitted portion of the ray leaves the interface, its TE and TM directions are given by

$$\widehat{\mathrm{TE}}_{t0} = \hat{k}_{t0}\times\hat{n}_0/\sin\theta_{t0}, \qquad \widehat{\mathrm{TM}}_{t0} = \widehat{\mathrm{TE}}_{t0}\times\hat{k}_{t0}. \tag{21}$$

As this interior ray approaches the $p = 1$ interface, the incident-wave-vector and polarization states are

$$\hat{k}_{i1} = \hat{k}_{t0}, \tag{22}$$

$$\widehat{\mathrm{TE}}_{i1} = \hat{k}_{i1}\times\hat{n}_1/\sin\theta_{i1}, \qquad \widehat{\mathrm{TM}}_{i1} = \widehat{\mathrm{TE}}_{i1}\times\hat{k}_{i1}, \tag{23}$$

respectively, where $\hat{n}_1$ is the unit outward normal to the cylinder at the interaction point (x_1, y_1, z_1). The $\widehat{\mathrm{TE}}_{i1}$ and $\widehat{\mathrm{TM}}_{i1}$ directions are rotated with respect to the $\widehat{\mathrm{TE}}_{t0}$ and $\widehat{\mathrm{TM}}_{t0}$ directions for $\xi \neq 0$ by

$$\begin{pmatrix}\widehat{\mathrm{TM}}_{i1}\\ \widehat{\mathrm{TE}}_{i1}\end{pmatrix} = R(\eta)\begin{pmatrix}\widehat{\mathrm{TM}}_{t0}\\ \widehat{\mathrm{TE}}_{t0}\end{pmatrix}, \tag{24}$$

where

$$\cos\eta = (\sin^2\phi_{t0} - \sin^2\gamma\cos^2\phi_{t0})/\sin^2\theta_{t0},$$

$$\sin\eta = \sin\gamma\sin(2\phi_{t0})/\sin^2\theta_{t0}. \tag{25}$$

The continued propagation of the ray through the cylinder proceeds in a similar way. Each transmission and reflection is diagonal in the local TE and TM basis, and the TE and TM directions are rotated by the angle η between successive interactions. The polarization of the final p-scattered ray is then

$$\begin{pmatrix}E^{\epsilon}_{rp}\\ E^{\mu}_{rp}\end{pmatrix} = R(-\chi)\begin{bmatrix}r^{\mathrm{TM}}_0 & 0\\ 0 & r^{\mathrm{TE}}_0\end{bmatrix}R(-\chi)\begin{pmatrix}E^{\epsilon}_0\\ E^{\mu}_0\end{pmatrix} \qquad \text{for } p = 0,$$

$$\begin{pmatrix}E^{\epsilon}_{tp}\\ E^{\mu}_{tp}\end{pmatrix} = R(-\chi)\begin{bmatrix}t^{\mathrm{TM}}_p & 0\\ 0 & t^{\mathrm{TE}}_p\end{bmatrix}\left\{\prod_{j=1}^{p-1}R(\eta)\begin{bmatrix}r^{\mathrm{TM}}_j & 0\\ 0 & r^{\mathrm{TE}}_j\end{bmatrix}\right\}R(\eta) \times\begin{bmatrix}t^{\mathrm{TM}}_0 & 0\\ 0 & t^{\mathrm{TE}}_0\end{bmatrix}R(-\chi)\begin{pmatrix}E^{\epsilon}_0\\ E^{\mu}_0\end{pmatrix} \qquad \text{for } p \geq 1, \tag{26}$$

in agreement with the result obtained by Takano and Tanaka,[37] and the polarization state of the p-interior ray is

$$\begin{pmatrix}E^{\epsilon}_{\mathrm{interior},p}\\ E^{\mu}_{\mathrm{interior},p}\end{pmatrix} = R(\sigma)\left\{\prod_{j=1}^{p-1}\begin{bmatrix}r^{\mathrm{TM}}_j & 0\\ 0 & r^{\mathrm{TE}}_j\end{bmatrix}R(\eta)\right\} \times\begin{bmatrix}t^{\mathrm{TM}}_0 & 0\\ 0 & t^{\mathrm{TE}}_0\end{bmatrix}R(-\chi)\begin{pmatrix}E^{\epsilon}_0\\ E^{\mu}_0\end{pmatrix}, \tag{27}$$

where

$$\cos\sigma = \sin\phi_{t0}/\sin\theta_{t0},$$

$$\sin\sigma = \sin\gamma\cos\phi_{t0}/\sin\theta_{t0}, \tag{28}$$

in analogy to Eqs. (17). As mentioned briefly in Subsection 2.A, both polarization-preserving scattering (ϵ incident goes to ϵ scattered or interior, and μ incident goes to μ scattered or interior) and cross-polarized scattering (ϵ incident goes to μ scattered or interior, and μ incident goes to ϵ scattered or interior) occur for $\xi \neq 0$ because (1) the ϵ and μ polarization states are mixtures of TE and TM polarization states (i.e., $\chi \neq 0$), (2) the TE and TM Fresnel coefficients are unequal, and (3) the planes of incidence at successive interactions of the ray with the surface do not coincide (i.e., $\eta \neq 0$).

3. INTERIOR AND EXTERIOR CAUSTICS IN RAY THEORY

Because the projection in the x–y plane of the set of ray trajectories for scattering of a plane wave with tilt angle ξ by a cylinder of refractive index n is identical to the set of trajectories for scattering at normal incidence with refractive index n', the types of caustics that occur for both geometries are identical. The interior caustics are cusps with the cusp point focal lines occurring at[15]

$$x = \frac{(-1)^p}{2p - 1 - n'}\,a, \qquad y = 0 \tag{29}$$

for all values of z. The exterior caustics consist of a $p = 1$ near-zone cylindrical aberration cusp caustic, whose cusp point focal line occurs at

$$x = \frac{n'a}{2(n' - 1)}, \qquad y = 0 \tag{30}$$

for all z, and far-zone rainbow caustics for $p \geq 2$ occurring at the scattering angle Θ in Eq. (11) with[5]

$$\cos\phi_{i0} = \left(\frac{n'^2 - 1}{p^2 - 1}\right)^{1/2}. \tag{31}$$

An interesting caustic transition occurs when $n' = 2.0$, corresponding to a plane wave with the tilt angle

$$\sin\xi_e = \left(\frac{4 - n^2}{3}\right)^{1/2}. \tag{32}$$

The tilt angle ξ_e is the value of ξ at this transition. As n' increases toward 2.0, the $p = 1$ near-zone cusp point focal line retracts toward the cylinder surface. At $n' = 2.0$ it touches the surface, and at $n' > 2.0$ it lies within the cylinder. This transition is shown in Fig. 3. Simultaneously, as n' increases toward 2.0, the two $p = 2$ rainbow branches to either side of the backscattered direction migrate toward $\Theta = 180°$. At $n' = 2.0$ the two branches join at $\Theta = 180°$, and for $n' > 2.0$ the first-order rainbow ceases to exist. The transitions of the $p = 1$ near-zone/interior caustic and the $p = 2$ far-zone rainbow are related. The $p = 2$ rainbow is formed by a turning point of the scattering angle Θ when considered as a function of ϕ_{i0}. As ξ increases, the turning point occurs at a smaller value of ϕ_{i0}. When $n' = 2.0$, it occurs at $\phi_{i0} = 0$. The $p = 1$ interior rays that form the cusp point focal line reflect straight back along the x axis of Fig. 1 as $p = 2$ interior rays and then exit the cylinder and form the $p = 2$ rainbow at $\Theta = 180°$. For $n' > 2.0$ the presence of the cusp point focal line inside the cylinder prevents the occurrence of a turning point of Θ for the $p = 2$ exterior rays.

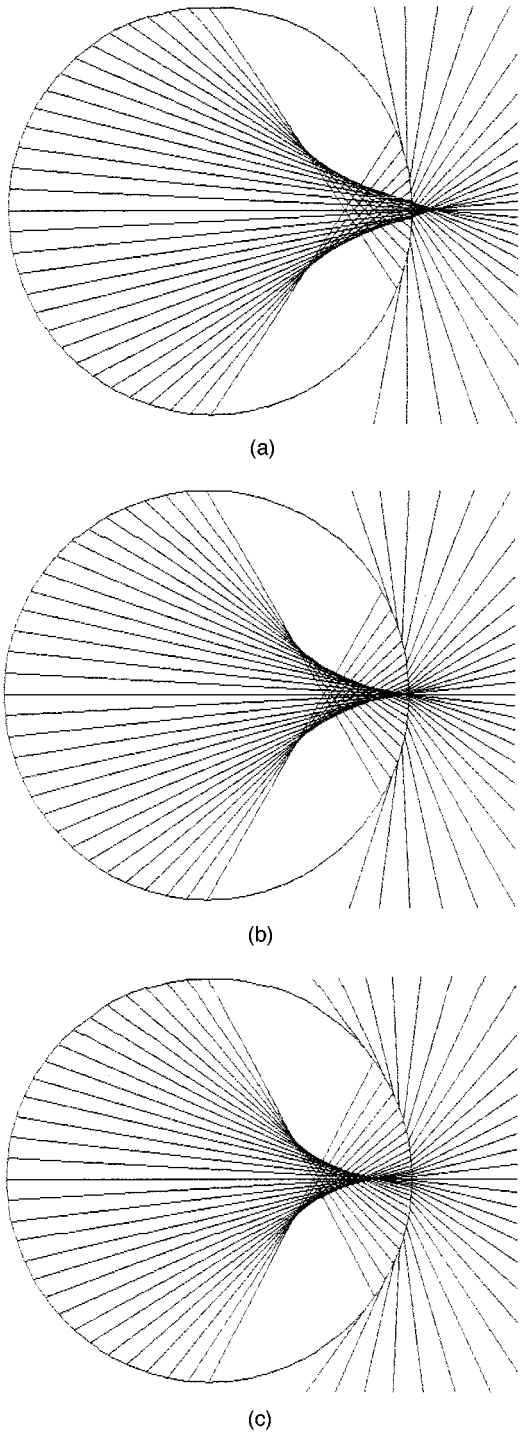

Fig. 3. $p = 1$ focusing caustic as seen from the top of the cylinder for (a) $n' = 1.807$, (b) $n' = 2.0$, and (c) $n' = 2.188$. These refractive indices were chosen so as to correspond to the experimental observations of Figs. 7(a), 7(b), and 7(c), respectively, below. For $n' < 2.0$ the cusp point focal line occurs outside the cylinder, and for $n' > 2.0$ it occurs inside the cylinder.

In Fig. 4 we illustrate the $1 \leqslant p \leqslant 5$ interior caustics for $n' = 2.0$. For $p \geqslant 3$ each caustic is a cusp whose focal line lies progressively closer to the z axis. The $p = 2$ caustic is the extension of the $p = 2$ rainbow inside the cylinder. The intensity of the paraxial rays that form the cusp point focal lines was calculated by using Eq. (27) for an unpolarized incident beam and for $n = 1.484$. The results are given in Table 1 for $1 \leqslant p \leqslant 6$ for normal incidence and for $\xi_e = 50.72°$, corresponding to $n' = 2.0$ as in Eq. (32). The much larger ray intensity for diagonal incidence is due to the increase in the internal-reflection Fresnel coefficient as ξ increases, which suggests the observability of high-order internal caustics under favorable circumstances. For a given value of p, the intensity as a function of ϕ_{i0} was found to peak sharply for rays incident near the edge of the cylinder. Also given in Table 1 are the highest-intensity member of the interior p-ray family for $\xi_e = 50.72°$ and the angle ϕ_{i0} at which this maximum occurs. These intense nonparaxial rays are expected to appear visually brighter than the cusp point focal lines produced by the paraxial rays, and they are examined further in Section 4.

4. EXPERIMENTAL OBSERVATION OF HIGH-ORDER INTERNAL CUSP CAUSTICS

The $\lambda = 0.6328$ μm unpolarized beam of a 15-mW HeNe laser was expanded to a diameter of 5.0 cm by a series of lenses. The expanded beam was incident on a glass rod[38] whose cross section was unintentionally slightly elliptical with a semimajor length $b = 7.8 \pm 0.05$ mm and a semiminor length $a = 7.5 \pm 0.05$ mm and whose overall length was 13.4 ± 0.05 cm. The sides of the rod were polished, and its ends were cut perpendicularly to the rod axis and frosted so as to make visible the interior caustics that intersected the ends of the cylinder. Visual inspection of the rod showed it to be free of inclusions and bubbles. Observation of the straightness of the first- and second-order rainbows at normal incidence provided evidence that the glass was free of major inhomogeneities, although shadow bands observed in the intense near-forward scattering indicated that weak local inhomogeneities were present in the glass.

The refractive index of the glass rod was determined as follows. With the expanded laser beam at normal incidence, the rod was rotated until the major axis of its

slightly elliptical cross section was parallel to the beam (i.e., the end-on incidence orientation). Since the scattering angle of the second-order rainbow (i.e., $p = 3$) was found to be near 270° for this orientation, the position of the second-order rainbow is relatively insensitive to both the degree of ellipticity of the rod's cross section and the precise orientation of the major axis.[39] The second-order rainbow scattering angle was then measured 60 cm away from the rod. This angle was corrected for the rod ellipticity[39] and the curvature of the rainbow caustic[13] as it progresses from the near zone to the far zone. The refractive index was then determined from the corrected $p = 3$ normal-incidence rainbow angle. We obtained

$$n = 1.484 \pm 0.002. \tag{33}$$

The glass rod was then mounted on an aluminum bracket, which in turn was affixed to a rotation stage so that the bracket axis and the rotation axis of the stage coincided. This allowed the tilt angle ξ, after being calibrated with respect to the propagation direction of the laser beam, to be read on the rotation stage angular grid scale. The major axis of the rod's slightly elliptical cross section was then oriented so that it, the rod axis, and the incident beam all lay in the same plane. All experimental observations were made in this orientation.

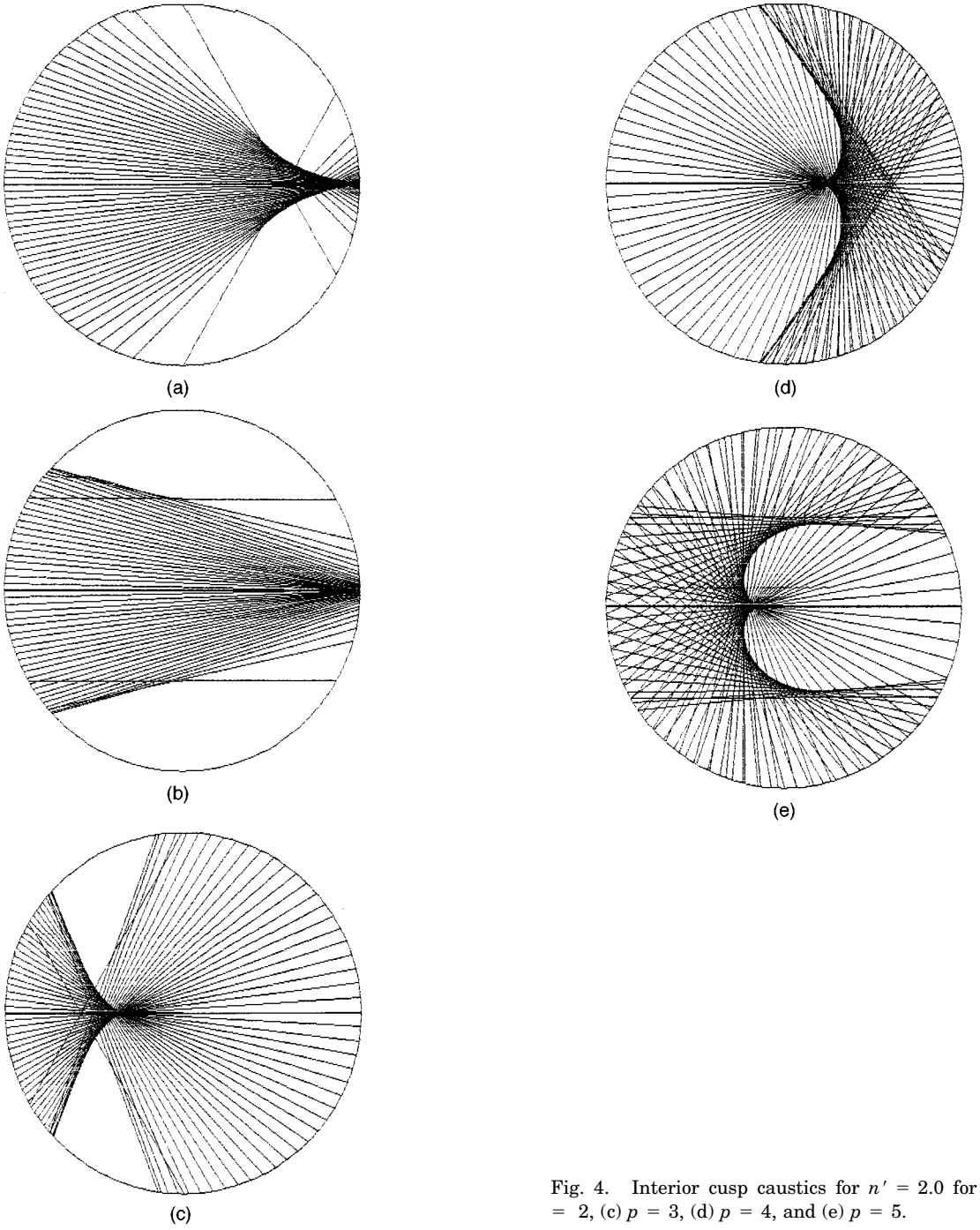

Fig. 4. Interior cusp caustics for $n' = 2.0$ for (a) $p = 1$, (b) $p = 2$, (c) $p = 3$, (d) $p = 4$, and (e) $p = 5$.

Table 1. Intensity of the Paraxial Rays $[I(\phi_{i0} = 0)]$ Contributing to the Cusp Points, Angle of Incidence of the Rays with Maximum Intensity (ϕ_{i0}^{max}), and Maximum Ray Intensity (I^{max}) for Interior Ray Families $1 \leq p \leq 6$ at Normal Incidence and with Tilt Angle ξ_e Corresponding to $n' = 2.0$ for $n = 1.484$ and an Unpolarized Incident Beam

p	$\xi = 0.0°$ $I(\phi_{i0} = 0)$	$\xi_e = 50.72°$ $I(\phi_{i0} = 0)$	ϕ_{i0}^{max}	I^{max}
1	3.24×10^{-1}	2.36×10^{-1}	0.0°	2.36×10^{-1}
2	1.23×10^{-2}	1.26×10^{-2}	64.0°	2.40×10^{-2}
3	4.66×10^{-4}	1.37×10^{-3}	77.8°	6.57×10^{-3}
4	1.77×10^{-5}	1.52×10^{-4}	80.8°	3.63×10^{-3}
5	6.73×10^{-7}	1.69×10^{-5}	83.2°	2.06×10^{-3}
6	2.55×10^{-8}	1.88×10^{-6}	84.3°	1.43×10^{-3}

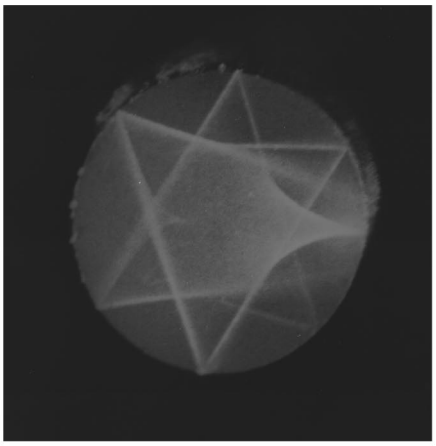

(a)

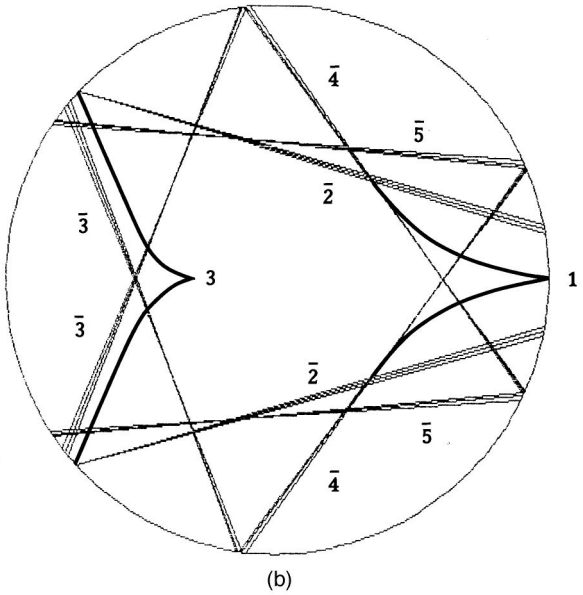

(b)

Fig. 5. (a) Photograph of the rod's upper frosted end at $\xi_e = 45°$ at which the $p = 1$ cusp point focal line touches the rod surface. (b) Composite of the $p = 1$ and 3 caustics and the $2 \leq \bar{p} \leq 5$ noncaustic ray trajectories over a 4° interval centered on the highest-intensity member of the interior p-ray family.

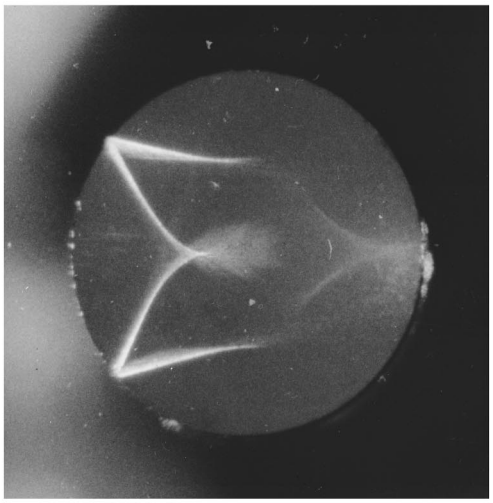

(a)

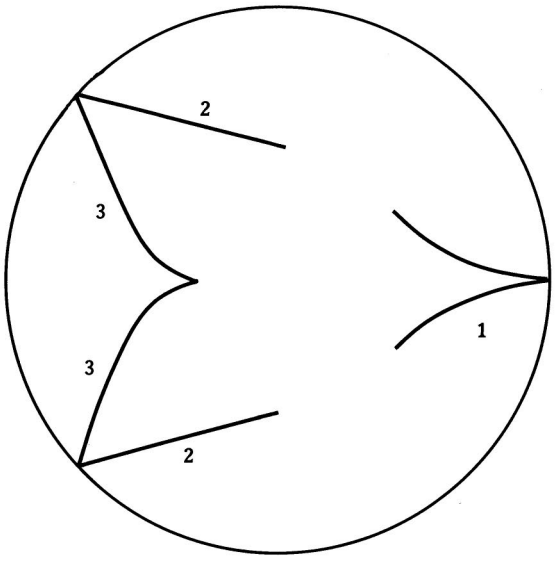

(b)

Fig. 6. (a) Photograph of the rod's upper frosted end at $\xi_e = 45°$ and with two black cards blocking all but a relatively narrow band near the top of the rod. (b) Composite of the $1 \leq p \leq 3$ caustics.

We made four sets of observations of the rod's interior caustics with this apparatus by photographing the upper frosted end of the rod. First, illuminating the rod with the expanded laser beam, we varied the rod tilt angle until the $p = 1$ cusp focal line touched the rod surface. This occurred at $\xi_e = 45° \pm 1°$, and a photograph of the rod's upper frosted end at this tilt angle is shown as Fig. 5(a). Although the $p = 1$ cusp of Fig. 4(a) and the $p = 3$ cusp of Fig. 4(c) are easily recognized in Fig. 5(a), the bright straight lines in the photograph that together form a six-sided star pattern do not correspond to any of the interior caustics of Fig. 4. Rather, they are the trajectories of the highest-intensity member of a number of interior p-ray families as given in Table 1. We denote these bright noncaustic ray trajectories by $\bar{p}$. In Fig. 5(b) these trajectories are illustrated for a 4° interval centered on the highest-intensity ray for $2 \leq \bar{p} \leq 5$ in order to simu-

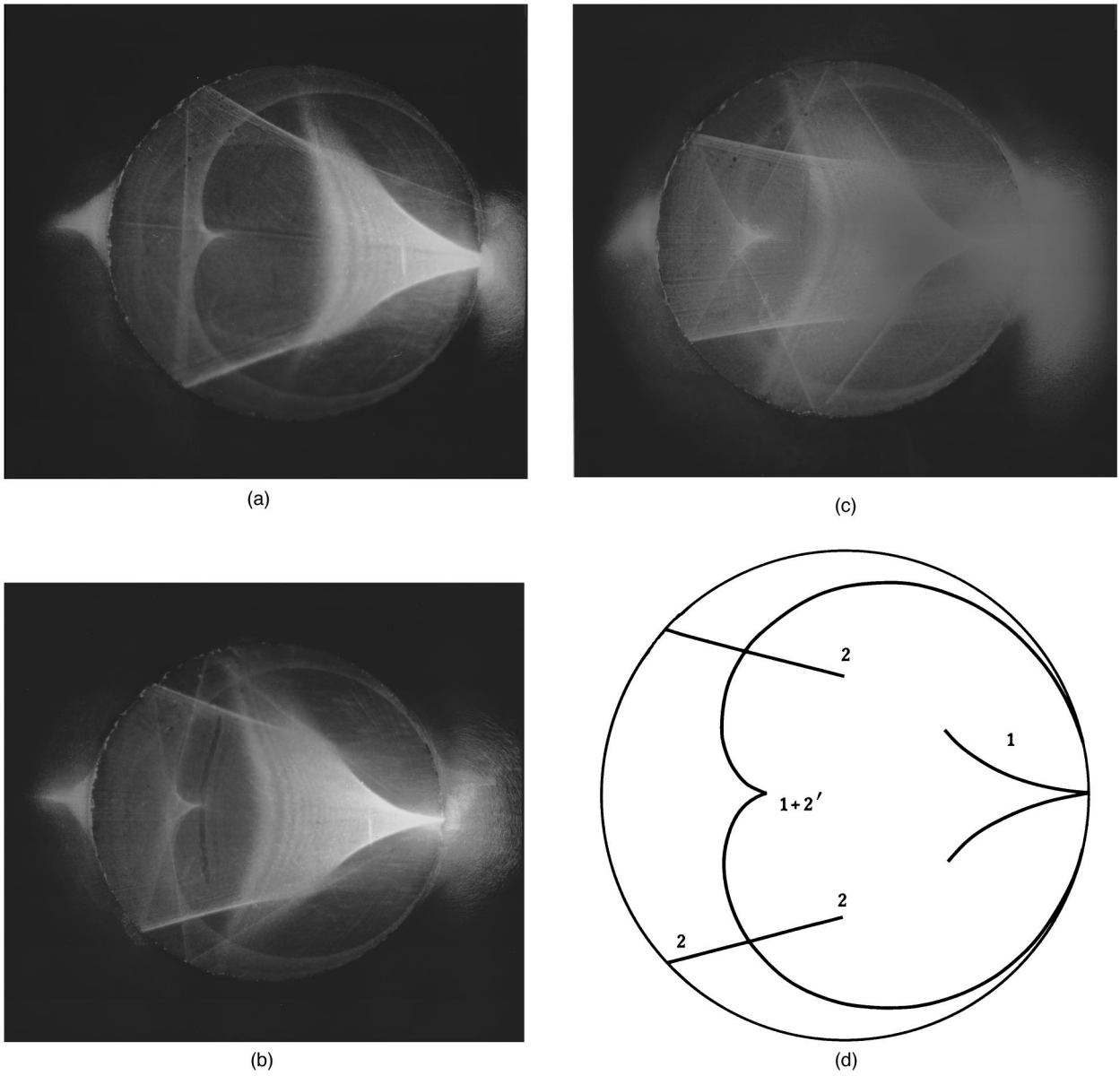

Fig. 7. Unfolding of the $p = 1$ cusp caustic for (a) $\xi = 38°$, (b) $\xi_e = 45°$, and (c) $\xi = 50°$. A composite of the $p = 1$ and 2 caustics for $n' = 2.0$ and the interior line source $1 + 2'$ caustic is illustrated in (d) and is to be compared with the photograph in (b).

late the sharp peaking of the interior ray intensity as a function of ϕ_{i0} as mentioned in Section 3. The $p = 1$ and 3 cusp caustics are also illustrated in Fig. 5(b). Together, the $p = 1$ and 3 cusps and the $2 \leqslant \bar{p} \leqslant 5$ noncaustic ray trajectories well describe the observations of Fig. 5(a).

According to Eq. (32) and assuming that the cylinder's cross section is circular, the $p = 1$ cusp point focal line should touch the rod surface at $\xi_e = 50.72°$, and not at $\xi_e = 45°$ as was observed. For a cylinder with an elliptical cross section and illuminated by the laser beam in the end-on orientation, the $p = 1$ cusp point focal line touches the cylinder surface when the $p = 1$ interaction of the paraxial rays with the cylinder surface occurs on the ellipse major axis. A calculation of this ellipticity effect gave the tilt angle as

$$\cos \xi_e = \left(\frac{b}{a}\right)\left(1 - \frac{a^2}{2b^2}\right)\left(1 - \frac{a^2}{4b^2}\right)^{-1/2}(n^2 - 1)^{1/2}. \tag{34}$$

Substitution of $n = 1.484$ and $b/a = 1.04$ into Eq. (34) yields $\xi_e = 45.68°$, in agreement with the experimental tilt angle.

For the three other sets of observations, a black card was placed in the expanded beam so as to block off the rays striking either the upper or lower portion of the rod. Because the interior rays walk up the rod through successive internal reflections at the angle γ, only rays with small p values intersected the upper frosted end of the rod when the lower portion of the rod was blocked. Similarly, only rays with large p values intersected the upper

frosted end when the upper portion of the rod was blocked. This beam-blocking technique is analogous to Walker's technique for observing high-order sphere glare spots and allowed us to choose certain p caustics selectively for examination. In our second set of observations, two blocking cards were employed so as to illuminate only a relatively narrow band near the top of the rod. This selected only the $1 \leqslant p \leqslant 3$ caustics of Figs. 4(a)–4(c), which appear in the photograph of Fig. 6(a). A composite of these three caustics from Figs. 4(a)–4(c) is also illustrated as Fig. 6(b).

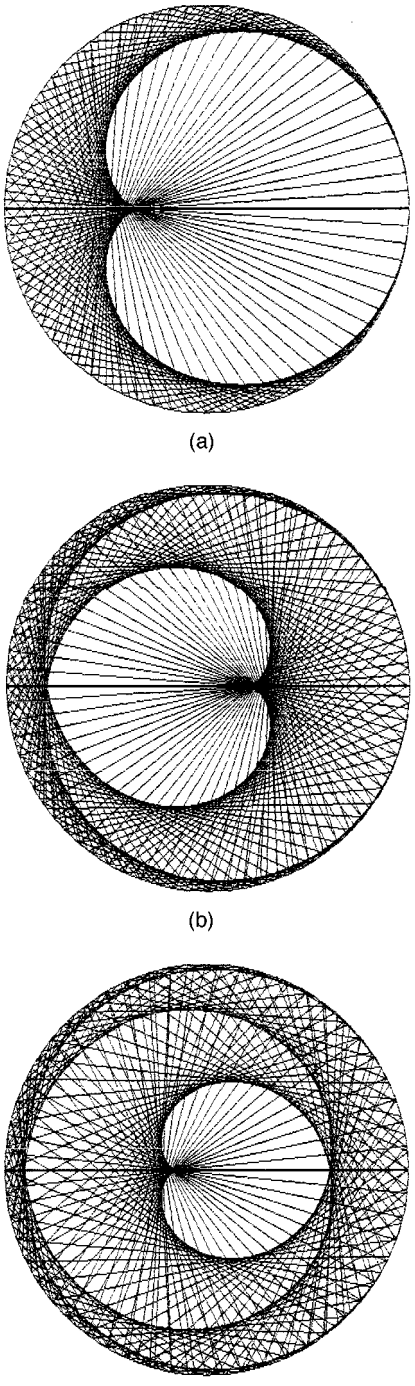

Fig. 8. Interior line source caustics $1 + p'$ for (a) $p' = 2$, (b) $p' = 3$, and (c) $p' = 4$.

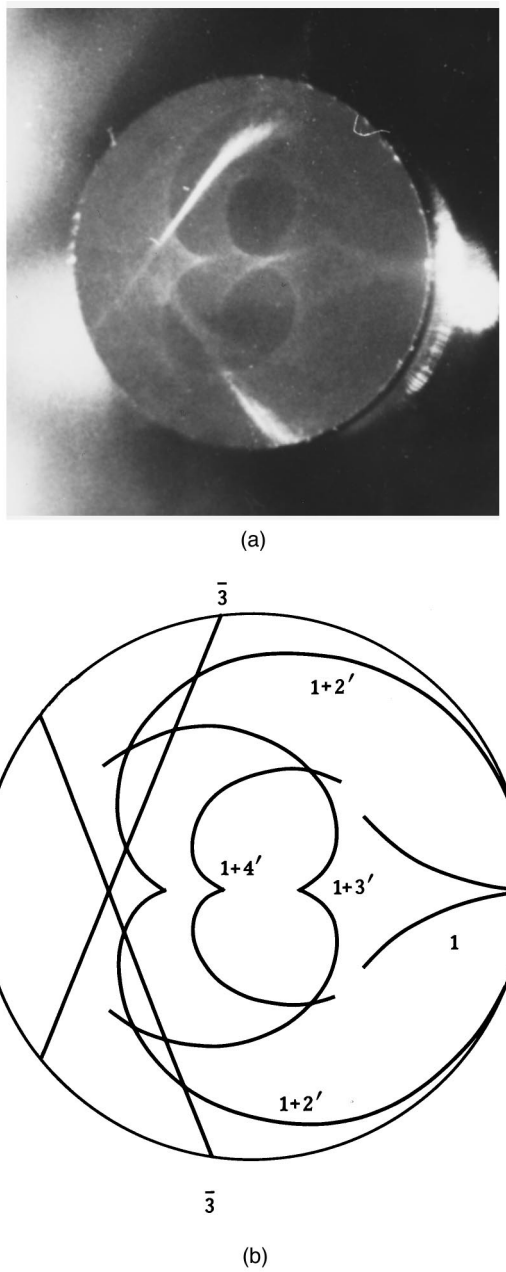

Fig. 9. (a) Photograph of the rod's upper frosted end at $\xi_e = 45°$ and with a black card blocking only the very top of the rod. (b) Composite of the $p = 1$ caustic, and $\bar{3}$ noncaustic ray trajectory, and the $1 + p'$ interior line source caustics for $2 \leqslant p' \leqslant 4$.

The lower portion of the rod was blocked for our next set of observations, in which the unfolding of the $p = 1$ cusp caustic was monitored as a function of ξ. Figures 7(a), 7(b), and 7(c) show the $p = 1$ caustic for $\xi = 38°$, 45°, and 50°, respectively. These results closely match the predicted unfolding in Figs. 3(a), 3(b), and 3(c), where we employed $n' = 1.807$, $n' = 2.0$, and $n' = 2.188$, respectively. These effective indices correspond to tilt angles 7° lower and 5° higher than $\xi_e = 50.72°$ for $n' = 2.0$. These values were chosen so as to correct our circular cross-section calculations approximately back to the elliptical cross-section photographs that also correspond to 7° below ξ_e, at ξ_e, and 5° above ξ_e. The photographs

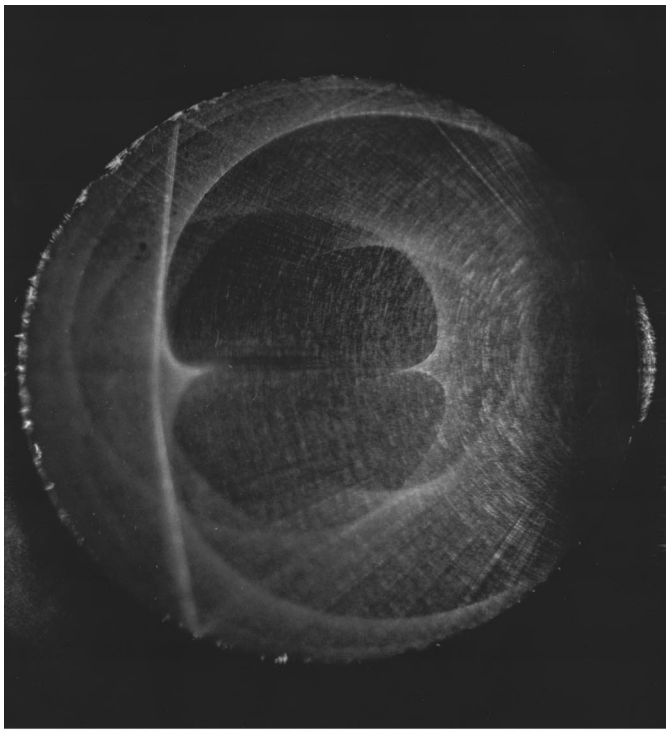

(a)

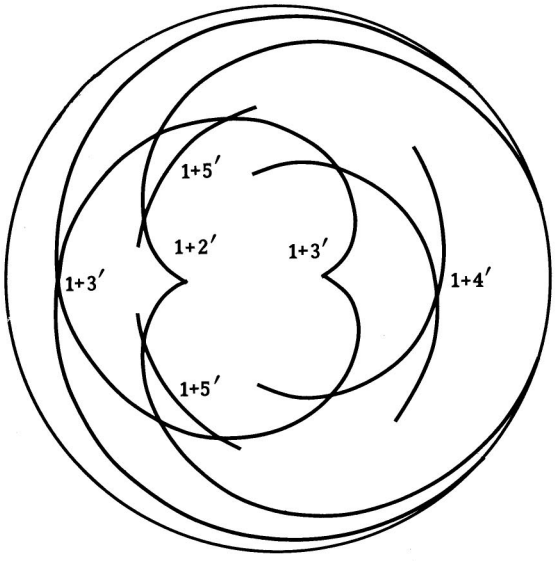

(b)

Fig. 10. (a) Photograph of the rod's upper frosted end at $\xi_e = 45°$ and with a black card blocking a substantial fraction of the upper portion of the rod. (b) Composite of the $1 + p'$ interior line source caustics for $2 \leqslant p' \leqslant 5$.

of Figs. 7(a)–7(c) illustrate another interesting phenomenon as well. Figure 7(b), for example, clearly shows the $p = 1$ and 2 caustics of Figs. 4(a) and 4(b). The remaining cusp, however, is not the $p = 3$ cusp of Fig. 4(c). The cusp point focal line is in the correct location. But the cusp's curving arms extend all the way around the rod to the $p = 1$ cusp point focal line rather than proceeding directly to the rod surface as in Figs. 4(c) and 6(a). This anomalous cusp caustic matches the one-internal-reflection caustic of a line source located on the rod surface that radiates in all directions. Evidently, the strongly focused $p = 1$ light at the surface is scattered in all directions by weak local inhomogeneities of the glass or small imperfections at its surface such as the adherence of a small amount of dust or fingerprints. We denote these interior line source caustics by $1 + p'$, since they have p' internal chords after leaving the effective line source that was produced by the $p = 1$ ray focusing. In Fig. 8 we illustrate the $1 + p'$ caustics for $2 \leqslant p' \leqslant 4$. Analytical equations for the shape of these caustics for an arbitrary location of the internal source were also derived by using the method employed in Appendix A of Ref. 15. Figure 7(d) shows a composite of the 1, 2, and $1 + 2'$ interior caustics. This composite well describes the experimental observations of Fig. 7(b). In Fig. 7(a) the $p = 1$ and 2 caustics are visible, as well as the interior source caustic $1 + 2'$ and the noncaustic ray trajectory $\bar{3}$. In Fig. 7(c) both the $p = 3$ and $1 + 2'$ caustics are visible and emanate from the same cusp point focal line. The $\bar{3}$ and $\bar{4}$ noncaustic ray trajectories are also visible. The interior source mechanism may also contribute in part to the lit-side internal SRS hot spot for a sphere,[2] with the shadow-side SRS hot spot acting as the internal source.

Because the position of the cusp point focal line of the p caustic coincides with that of the corresponding $1 + p'$ caustic when the effective line source is on the rod surface, the only way to distinguish between these two caustics is to view the different paths of their curving arms. This is what motivated our final set of observations. We blocked off the top portion of the rod so as to observe high-p caustics. For the card blocking only the very top of the rod, a photograph of the resulting caustics is shown as Fig. 9(a). The composite illustration of Fig. 9(b) identifies them as being the $p = 1$ cusp, the noncaustic trajectory $\bar{3}$, and the $1 + p'$ interior line source caustics for $2 \leqslant p' \leqslant 4$. Last, a photograph of the caustics that appear when a substantial portion of the top of the rod is blocked is shown as Fig. 10(a). The composite illustration of Fig. 10(b) identifies them as the $1 + p'$ interior line source caustics for $2 \leqslant p' \leqslant 5$. The six-internal-chord caustic $1 + 5'$, which is weakly but clearly visible in Fig. 10(a), is the highest-order caustic that we observed. The appearance in Fig. 10(a) of the crossing of the two curving arms of the $1 + 3'$ caustic and a similar crossing of the arms of the $1 + 4'$ caustic are also noteworthy. By variation of the cylinder tilt angle and the positions of one or two blocking cards, a wide variety of caustics and noncaustic ray trajectories may be seen. The effects that we have shown in Figs. 5–7, 9, and 10 provide only a sampling of what may be observed.

5. CONCLUSION

In Section 1 we noted that there has been much less investigation of the caustics of plane-wave/cylinder scattering than there has been of plane-wave/sphere and plane-wave/spheroid scattering, and perhaps this neglect was due to the expectation that nothing really new would be seen. Our experimental observations of Section 4 show that this is in fact not the case. When we peer into the

world of the interior of a glass rod illuminated at diagonal incidence, we do observe the expected interior caustics, but we observe much more as well. Because the internal-reflection Fresnel coefficients at diagonal incidence are much larger than those at normal incidence, we are able to see relatively high-order caustics. Because these reflection Fresnel coefficients peak strongly over a narrow range of ray impact parameters near the edge of the cylinder, individual noncaustic ray trajectories become visible as well. Because our glass rod has small imperfections at its surface and weak inhomogeneities of the glass, yet another class of caustics appears. In summary, light scattering of a diagonally incident plane wave by a slightly imperfect circular cylinder is a system rich in phenomena that have clear intuitive interpretations.

REFERENCES AND NOTES

1. E. Hecht, *Optics*, 2nd ed. (Addison-Wesley, Reading, Mass., 1987), p. 222, Fig. 6.13.
2. D. S. Benincasa, P. W. Barber, J.-Z. Zhang, W.-F. Hsieh, and R. K. Chang, "Spatial distribution of the internal and near-field intensities of large cylindrical and spherical scatterers," Appl. Opt. **26**, 1348–1356 (1987).
3. K. Sassen, "Angular scattering and rainbow formation in pendant drops," J. Opt. Soc. Am. **69**, 1083–1089 (1979).
4. C. W. Chan and W. K. Lee, "Measurement of a liquid refractive index by using high-order rainbows," J. Opt. Soc. Am. B **13**, 532–535 (1996).
5. J. D. Walker, "Multiple rainbows from single drops of water and other liquids," Am. J. Phys. **44**, 421–433 (1976).
6. J. D. Walker, "How to create and observe a dozen rainbows in a single drop of water," Sci. Am. **237**(1), 138–144 (1977).
7. J. D. Walker, "Mysteries of rainbows, notably their rare supernumerary arcs," Sci. Am. **242**(6), 174–184 (1980).
8. J. A. Lock, "Contribution of high-order rainbows to the scattering of a Gaussian laser beam by a spherical particle," J. Opt. Soc. Am. A **10**, 693–706 (1993).
9. J. A. Lock, "Theory of the observations made of high-order rainbows from a single water droplet," Appl. Opt. **26**, 5291–5298 (1987).
10. H. C. van de Hulst and R. T. Wang, "Glare points," Appl. Opt. **30**, 4755–4763 (1991).
11. C. F. Bohren and A. B. Fraser, "Newton's zero-order rainbow: unobservable or nonexistent," Am. J. Phys. **59**, 325–326 (1991).
12. A. E. Shapiro, "Comment on Newton's zero-order rainbow: unobservable or nonexistent," Am. J. Phys. **60**, 749–750 (1992).
13. J. A. Lock and T. A. McCollum, "Further thoughts on Newton's zero-order rainbow," Am. J. Phys. **62**, 1082–1089 (1994).
14. V. Srivastava and M. A. Jarzembski, "Laser-induced stimulated Raman scattering in the forward direction of a droplet: comparison of Mie theory with geometrical optics," Opt. Lett. **16**, 126–128 (1991).
15. J. A. Lock and E. A. Hovenac, "Internal caustic structure of illuminated liquid droplets," J. Opt. Soc. Am. A **8**, 1541–1552 (1991).
16. H. M. Lai, P. T. Leung, K. L. Poon, and K. Young, "Characterization of the internal energy density in Mie scattering," J. Opt. Soc. Am. A **8**, 1553–1558 (1991).
17. D. Q. Chowdhury, P. W. Barber, and S. C. Hill, "Energy-density distribution inside large nonabsorbing spheres using Mie theory and geometrical optics," Appl. Opt. **31**, 3518–3523 (1992).
18. M. A. Jarzembski and V. Srivastava, "Electromagnetic field enhancement in small liquid droplets using geometrical optics," Appl. Opt. **28**, 4962–4965 (1989).
19. J.-G. Xie, T. E. Ruekgauer, J. Gu, R. L. Armstrong, and R. G. Pinnick, "Observations of Descartes ring stimulated Raman scattering in micrometer-sized water droplets," Opt. Lett. **16**, 1310–1312 (1991).
20. P. Chylek, M. A. Jarzembski, N. Y. Chou, and R. G. Pinnick, "Effect of size and material of liquid spherical particles on laser-induced breakdown," Appl. Phys. Lett. **49**, 1475–1477 (1986).
21. R. G. Pinnick, P. Chylek, M. Jarzembski, E. Creegan, V. Srivastava, G. Fernandez, J. D. Pendleton, and A. Biswas, "Aerosol-induced laser breakdown thresholds: wavelength dependence," Appl. Opt. **27**, 987–996 (1988).
22. J. F. Nye, "Rainbow scattering from spheroidal drops—an explanation of the hyperbolic umbilic foci," Nature (London) **312**, 531–532 (1984).
23. J. F. Nye, "Rainbows from ellipsoidal water drops," Proc. R. Soc. London, Ser. A **438**, 397–417 (1992).
24. P. L. Marston and E. H. Trinh, "Hyperbolic umbilic diffraction catastrophe and rainbow scattering from spheroidal drops," Nature (London) **312**, 529–531 (1984).
25. P. L. Marston, "Cusp diffraction catastrophe from spheroids: generalized rainbows and inverse scattering," Opt. Lett. **10**, 588–590 (1985).
26. H. J. Simpson and P. L. Marston, "Scattering of white light from levitated oblate water drops near rainbows and other diffraction catastrophes," Appl. Opt. **30**, 3468–3473, 3547 (1991).
27. G. Kaduchak, P. L. Marston, and H. J. Simpson, "E_6 diffraction catastrophe of the primary rainbow of oblate water drops: observations with white-light and laser illumination," Appl. Opt. **33**, 4691–4696 (1994).
28. G. Kaduchak and P. L. Marston, "Hyperbolic umbilic and E_6 diffraction catastrophes associated with the secondary rainbow of oblate water drops: observations with laser illumination," Appl. Opt. **33**, 4697–4701 (1994).
29. P. L. Marston and G. Kaduchak, "Generalized rainbows and unfolded glories of oblate drops: organization for multiple internal reflections and extension of cusps into Alexander's dark band," Appl. Opt. **33**, 4702–4713 (1994).
30. J. A. Lock, "Ray scattering by an arbitrarily oriented spheroid. II. Transmission and cross-polarization effects," Appl. Opt. **35**, 515–531 (1996).
31. J. F. Owen, R. K. Chang, and P. W. Barber, "Internal electric field distributions of a dielectric cylinder at resonance wavelengths," Opt. Lett. **6**, 540–542 (1981).
32. A. Steinhardt and L. Fukshansky, "Geometrical optics approach to the intensity distribution infinite cylindrical media," Appl. Opt. **26**, 3778–3789 (1987).
33. J. A. Lock and C. L. Adler, "Debye-series analysis of the first-order rainbow produced in scattering of a diagonally incident plane wave by a circular cylinder," J. Opt. Soc. Am. A **14**, 1316–1328 (1997).
34. J. B. Keller and H. B. Keller, "Determination of reflected and transmitted fields by geometrical optics," J. Opt. Soc. Am. **40**, 48–52 (1950).
35. M. Kerker, *The Scattering of Light and Other Electromagnetic Radiation* (Academic, New York, 1969), p. 264, Fig. 6.3.
36. C. F. Bohren and D. R. Huffman, *Absorption and Scattering of Light by Small Particles* (Wiley, New York, 1983), p. 200, Fig. 8.4.
37. Y. Takano and M. Tanaka, "Phase matrix and cross sections for single scattering by circular cylinders: a comparison of ray optics and wave theory," Appl. Opt. **19**, 2781–2793 (1980).
38. The glass cylinder was provided, polished, and frosted by Ferguson's Cut Glass Originals, 4292 Pearl Road, Cleveland, Ohio 44109.
39. G. P. Können, "Appearance of supernumeraries of the secondary rainbow in rain showers," J. Opt. Soc. Am. A **4**, 810–816 (1987).